JFM RAPIDS
journals.cambridge.org/rapids

Liquid velocity fluctuations and energy spectra in three-dimensional buoyancy-driven bubbly flows

Vikash Pandey[1], Rashmi Ramadugu[1] and Prasad Perlekar[1,†]

[1]TIFR Centre for Interdisciplinary Sciences, Tata Institute of Fundamental Research, Hyderabad, 500107, India

We present a direct numerical simulation (DNS) study of pseudo-turbulence in buoyancy-driven bubbly flows for a range of Reynolds ($150 \leqslant Re \leqslant 546$) and Atwood ($0.04 \leqslant At \leqslant 0.9$) numbers. We study the probability distribution function of the horizontal and vertical liquid velocity fluctuations and find them to be in quantitative agreement with the experiments. The energy spectrum shows a k^{-3} scaling at high Re and becomes steeper on reducing Re. To investigate spectral transfers in the flow, we derive the scale-by-scale energy budget equation. Our analysis shows that, for scales smaller than the bubble diameter, the net transfer because of the surface tension and the kinetic energy flux balances viscous dissipation to give k^{-3} scaling of the energy spectrum for both low and high At.

Key words: bubble dynamics, multiphase flow, turbulence simulation

1. Introduction

Bubble-laden flow appears in a variety of natural (Clift, Grace & Weber 1978; Gonnermann & Manga 2007) and industrial (Deckwer 1992) processes. The presence of bubbles dramatically alters the transport properties of a flow (Mudde 2005; Ceccio 2010; Biferale *et al.* 2012; Pandit *et al.* 2017; Risso 2018; Alméras *et al.* 2019; Elghobashi 2019; Mathai, Lohse & Sun 2020). A single bubble of diameter d, because of buoyancy, rises under gravity. Its trajectory and the wake flow depend on the density and viscosity contrast with the ambient fluid, as well as the surface tension (Clift *et al.* 1978; Bhaga & Weber 1981; Tripathi, Sahu & Govindarajan 2015). A suspension of such bubbles at moderate volume fractions generates complex spatiotemporal flow patterns that are often referred to as pseudo-turbulence or bubble-induced agitation (Mudde 2005; Risso 2018).

Experiments have made significant progress in characterizing velocity fluctuations of the fluid phase in pseudo-turbulence. A key observation is the robust power-law

† Email address for correspondence: perlekar@tifrh.res.in

scaling in the energy spectrum, with an exponent of -3 either in frequency ν or the wavenumber k space (Mercado *et al.* 2010; Riboux, Risso & Legendre 2010; Mendez-Diaz *et al.* 2013). The scaling range, however, remains controversial. Riboux *et al.* (2010) investigated turbulence in the wake of a bubble swarm and found k^{-3} scaling for length scales larger than the bubble diameter d (i.e. $k < 2\pi/d$), whereas Mercado *et al.* (2010) and Prakash *et al.* (2016) observed this scaling for scales smaller than d in a steady-state bubble suspension. Experiments on buoyancy-driven bubbly flows in the presence of grid turbulence (Lance & Bataille 1991; Prakash *et al.* 2016; Alméras *et al.* 2017) observe Kolmogorov scaling for scales larger than the bubble diameter and smaller than the forcing scale, and a much steeper k^{-3} scaling for scales smaller than the bubble diameter and larger than the dissipation scale. Lance & Bataille (1991) argued that, assuming production because of wakes to be local in spectral space, balance of production with viscous dissipation leads to the observed k^{-3} scaling.

Fully resolved numerical simulations of three-dimensional bubbly flows for a range of Reynolds number $O(10) < Re < O(10^3)$ (Bunner & Tryggvason 2002a,b; Roghair *et al.* 2011) found k^{-3} scaling for length scales smaller than d ($k > 2\pi/d$), and attributed it to the balance between viscous dissipation and energy production by the wakes (Lance & Bataille 1991).

Two mechanisms proposed to explain the observed scaling behaviour in experiments are: (i) superposition of velocity fluctuations generated in the vicinity of the bubbles (Risso 2011) and (ii) at high Re, instabilities in the flow through bubble swarms (Lance & Bataille 1991; Mudde 2005; Risso 2018). In an experiment or a simulation, it is difficult to disentangle these two mechanisms.

In classical turbulence, a constant flux of energy is maintained between the injection and dissipation scales (Frisch 1997; Pandit, Perlekar & Ray 2009). In pseudo-turbulence, on the other hand, it is not clear how the energy injected by buoyancy is transferred between different scales. In particular, the following key questions remain unanswered: (i) How do liquid velocity fluctuations and the pseudo-turbulence spectrum depend on the Reynolds number (Re)? (ii) What is the energy budget and the dominant balances? (iii) Is there an energy cascade (a non-zero energy flux)?

In this paper, we address all of the above questions for experimentally relevant Reynolds (Re) and Atwood (At) numbers. We first investigate the dynamics of an isolated bubble and show that the wake flow behind the bubble is in agreement with earlier experiments and simulations. Next, for a bubbly suspension we show that the liquid velocity fluctuations are in quantitative agreement with the experiments of Riboux *et al.* (2010) and the bubble velocity fluctuations are in quantitative agreement with the simulations of Roghair *et al.* (2011). We then proceed to derive the scale-by-scale energy budget equation and investigate the dominant balances for different Re and At. We find that for scales smaller than the bubble diameter, viscous dissipation balances net nonlinear transfer of energy because of advection and the surface tension to give a k^{-3} pseudo-turbulence spectrum. The dominant balances are robust and do not depend on the density contrast (At).

2. Model and numerical details

We study the dynamics of bubbly flow by using Navier–Stokes (NS) equations with a surface-tension force due to bubbles:

$$\rho \mathrm{D}_t \boldsymbol{u} = \nabla \cdot [2\mu \boldsymbol{S}] - \nabla p + \boldsymbol{F}^\sigma + \boldsymbol{F}^g, \qquad (2.1a)$$

runs	L	N	N_b	d	g	μ_f	$\phi\,\%$	Ga	At	Bo	Re	λ	τ_λ
R1	256	512	60	24	1.0	0.32	2.6	104	0.04	1.8	150	11.3	36.6
R2	256	512	60	24	1.0	0.20	2.6	166	0.04	1.0	298	9.88	26.3
R3	128	432	10	22	8.75	0.42	2.6	206	0.04	2.1	315	8.51	8.1
R4	128	432	10	22	10.5	0.32	2.6	296	0.04	1.9	462	7.35	6.1
R5	256	256	40	24	0.1	0.32	1.7	113	0.90	2.0	173	10.0	38.7
R6	256	256	40	24	1.0	0.32	1.7	345	0.80	2.4	465	8.12	7.7
R7	256	256	40	24	1.0	0.32	1.7	358	0.90	1.9	546	7.31	7.0

TABLE 1. Table of parameters used in our DNS. Here, $\delta\rho \equiv \rho_f - \rho_b$ is the density difference, $Ga \equiv \sqrt{\rho_f \delta\rho g d^3}/\mu_f$ is the Galilei number, $Bo \equiv \delta\rho g d^2/\sigma$ is the Bond number, $At = \delta\rho/(\rho_f + \rho_b)$ is the Atwood number, and $Re \equiv \rho_f V_0 d/\mu_f$ is the bubble Reynolds number, where V_0 is the rise velocity of an isolated bubble, $\lambda \equiv \sqrt{10\mu_f E/\rho_f \epsilon_\mu}$ is the integral length scale, and $\tau_\lambda \equiv \lambda/\sqrt{2E/3\rho_f}$ is the integral time scale.

$$\nabla \cdot \boldsymbol{u} = 0. \qquad (2.1b)$$

Here, $D_t = \partial_t + (\boldsymbol{u} \cdot \nabla)$ is the material derivative, $\boldsymbol{u} = (u_x, u_y, u_z)$ is the hydrodynamic velocity, p is the pressure, $\boldsymbol{S} \equiv (\nabla\boldsymbol{u} + \nabla\boldsymbol{u}^T)/2$ is the rate of deformation tensor, $\rho \equiv \rho_f c + \rho_b(1 - c)$ is the density, $\mu \equiv \mu_f c + \mu_b(1 - c)$ is the viscosity, ρ_f (ρ_b) is the fluid (bubble) density and μ_b (μ_f) is the bubble (fluid) viscosity. The value of the indicator function c is equal to zero in the bubble phase and unity in the fluid phase. The surface-tension force is $\boldsymbol{F}^\sigma \equiv \sigma\kappa\hat{\boldsymbol{n}}$, where σ is the coefficient of surface tension, κ is the curvature and $\hat{\boldsymbol{n}}$ is the normal to the bubble interface. $\boldsymbol{F}^g \equiv [\rho_a - \rho]g\hat{z}$ is the buoyancy force, where g is the acceleration due to gravity and $\rho_a \equiv [\int \rho(c)\,d\boldsymbol{x}]/L^3$ is the average density. For small Atwood numbers, we employ the Boussinesq approximation, whereby ρ on the left-hand side of (2.1*a*) is replaced by the average density ρ_a. Note that low Atwood numbers can be experimentally realized in near-critical binary fluids as well as mixtures of oil (Perlekar 2019; Shukla *et al.* 2019).

We solve the Boussinesq-approximated NS using a pseudo-spectral method (Canuto *et al.* 2012) coupled to a front-tracking algorithm (Tryggvason *et al.* 2001; Aniszewski *et al.* 2019) for bubble dynamics. Time marching is done using a second-order Adams–Bashforth scheme. For the non-Boussinesq NS, we use the open source finite-volume-front-tracking solver PARIS (Aniszewski *et al.* 2019).

We use a cubic periodic box of volume L^3 and discretize it with N^3 collocation points. We initialize the velocity field $\boldsymbol{u} = 0$ and place the centres of N_b bubbles at random locations such that no two bubbles overlap. The Reynolds number Re, Bond number Bo and bubble volume fraction $\phi \equiv [\int(1 - c)\,d\boldsymbol{x}]/L^3$ that we use (see table 1) are comparable to the experiments (Riboux *et al.* 2010; Mendez-Diaz *et al.* 2013).

3. Results

In subsequent sections, we investigate the statistical properties of stationary pseudo-turbulence generated in buoyancy-driven bubbly flows. Table 1 lists the parameters used in our simulations. Our parameters are chosen such that the Reynolds number, Bond number and volume fraction are comparable to those used in earlier experiments (Riboux *et al.* 2010; Mendez-Diaz *et al.* 2013; Risso 2018). We conduct simulations at both low and high *At* numbers to investigate the role of density
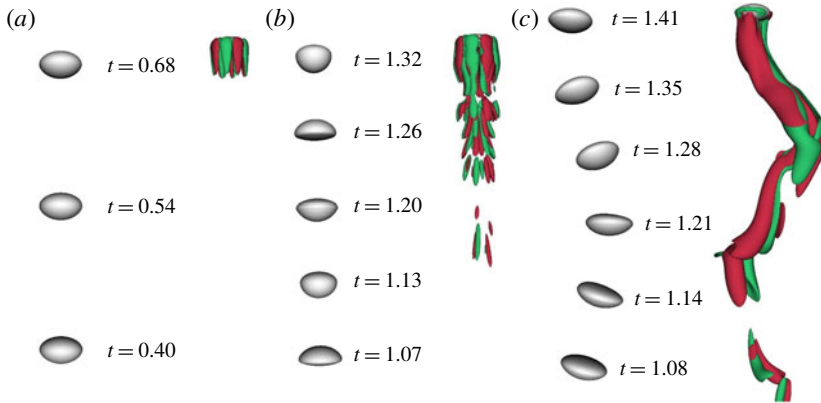
FIGURE 1. Bubble positions at different times (in units of $\tau_s \equiv L/\sqrt{\delta\rho g d/\rho_f}$) and the z-component of the vorticity ($\omega_z = \partial_x u_y - \partial_y u_x$) for the case of a single bubble rising under gravity. The non-dimensional parameters in representative cases are taken the same as run R1 in (*a*), run R4 in (*b*) and run R6 in (*c*). Green regions correspond to $\omega_z < 0$, whereas red regions correspond to $\omega_z > 0$. We plot iso-contours corresponding to $|\omega_z| = \pm 10^{-3}$ in (*a*), $|\omega_z| = \pm 10^{-2}$ in (*b*) and $|\omega_z| = \pm 10^{-1}$ in (*c*).

differences on the statistics of pseudo-turbulence. The rest of the paper is organized as follows. In § 3.1, we study the trajectory of an isolated bubble and, consistent with the experiments, show that the bubble shape is ellipsoidal. In §§ 3.2 and 3.3, we investigate the total kinetic energy budget and the fluid and bubble centre-of-mass velocity fluctuations, then make quantitative comparisons with the experiments. In § 3.4, we study the kinetic energy spectrum and scale-by-scale energy budget. In § 3.5, we investigate the length scale of pseudo-turbulence and, in § 3.6, we investigate the clustering of bubbles. We present our conclusions in § 4.

3.1. *Single bubble dynamics*

In this section, we study the dynamics of an initially spherical bubble as it rises because of buoyancy. The seminal work of Bhaga & Weber (1981), Wu & Gharib (2002) and Tchoufag, Magnaudet & Fabre (2014) characterized the shape and trajectory of an isolated bubble in terms of the Reynolds and Bond numbers. Experiments on turbulent bubbly flows (Lance & Bataille 1991; Prakash *et al.* 2016; Mathai *et al.* 2018) observe ellipsoidal bubbles. In the following, we characterize the dynamics of an isolated bubble for the parameters used in our simulations.

To avoid the interaction of the bubble with its own wake, we use a vertically elongated cuboidal domain of dimension $5d \times 5d \times 21d$. After the bubble rise velocity attains steady state, figure 1(*a–c*) shows the bubble shape and the vertical component of the vorticity $\omega_z = (\nabla \times \boldsymbol{u}) \cdot \hat{z}$. For $Re = 150$ and $At = 0.04$ (run R1), the bubble shape is an oblate ellipsoid and rises in a rectilinear trajectory. On increasing to $Re = 462$ (run R4), the bubble pulsates while rising and sheds varicose vortices similar to Pivello *et al.* (2014). Finally, for high $At = 0.80$ and $Re = 465$ (run R6), similar to region III of Tripathi *et al.* (2015), we find that the bubble shape is an oblate ellipsoid and follows a zigzag trajectory.
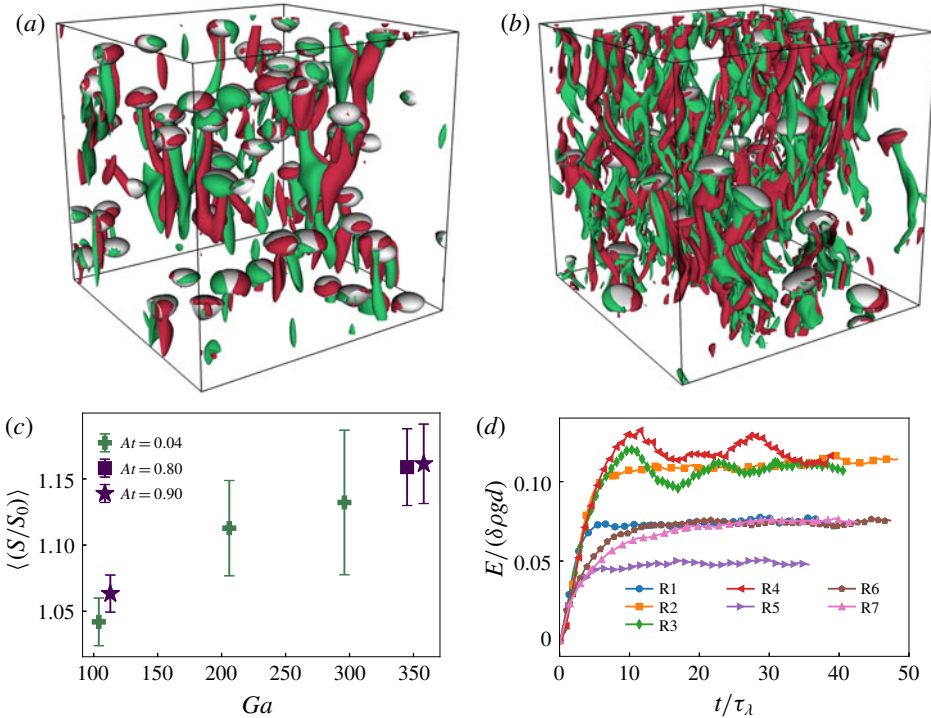
FIGURE 2. Representative steady-state snapshot of the bubbles overlaid on the iso-contour plots of the z-component of the vorticity field $\omega_z \equiv [\boldsymbol{\nabla} \times \boldsymbol{u}] \cdot \hat{\boldsymbol{z}}$ for $Re = 150$, $At = 0.04$ (*a*) and for $Re = 465$, $At = 0.8$ (*b*). Regions with $\omega_z = 2\sigma_\omega(-2\sigma_\omega)$ are shown in red (green), where σ_ω is the standard deviation of ω_z. As expected, bubble–wake interactions become more intense on increasing Re. (*c*) Average bubble deformation $\langle\langle S(t)/S(0)\rangle\rangle$ versus Ga for low and high At numbers. (*d*) Kinetic energy evolution for the runs given in table 1.

3.2. *Bubble suspension and kinetic energy budget*

The plots in figure 2(*a*,*b*) show the representative steady-state iso-vorticity contours of the z-component of the vorticity along with the bubble interface position for our bubbly flow configurations. As expected from our isolated bubble study in the previous section, we observe rising ellipsoidal bubbles and their wakes, which interact to generate pseudo-turbulence. The individual bubbles in the suspension show shape undulations which are similar to their isolated bubble counterparts (see movies available in the supplementary material at https://doi.org/10.1017/jfm.2019.991). Furthermore, for comparable $Bo \approx 2$, the average bubble deformation $\langle\langle S(t)/S(0)\rangle\rangle$ increases with increasing Re (figure 2*c*). Here, $\langle\langle \cdot \rangle\rangle$ denotes temporal averaging over bubble trajectories in the statistically steady state, $S(t)$ is the surface area of the bubble and $S(0) = \pi d^2$.

The time evolution of the kinetic energy $E = \langle \rho u^2/2 \rangle$ for runs R1–R7 is shown in figure 2(*d*). A statistically steady state is attained close to $t \approx 20\tau_\lambda$, where τ_λ is the integral time scale (see table 1). Using (2.1*a*), we obtain the balance equation for the
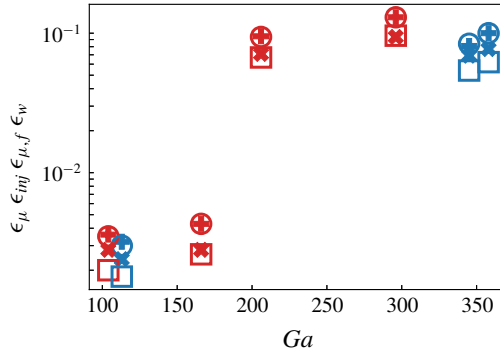
FIGURE 3. Energy dissipation rate ϵ_μ (filled plus), estimation of the liquid dissipation rate $\epsilon_w \equiv \phi(\delta\rho g d/\rho_f)^{3/2}/d$ (empty squares) because of the bubble wakes (Lance & Bataille 1991), dissipation rate in the fluid $\epsilon_{\mu,f}$ (filled cross) and energy injection rate ϵ_{inj} (empty circles) for runs R1–R7. The low-At runs are marked in red and the high-At runs are marked in blue.

total kinetic energy E as

$$\partial_t \underbrace{\left\langle \frac{\rho \boldsymbol{u}^2}{2} \right\rangle}_{E} = - \underbrace{2\langle \mu(c)\boldsymbol{S}:\boldsymbol{S}\rangle}_{\epsilon_\mu} + \underbrace{\langle [\rho_a - \rho(c)]u_y g\rangle}_{\epsilon_{inj}} + \underbrace{\langle \boldsymbol{F}^\sigma \cdot \boldsymbol{u}\rangle}_{\epsilon_\sigma}, \qquad (3.1)$$

where $\langle \cdot \rangle$ represents spatial averaging. In steady state, the energy injected by buoyancy ϵ_{inj} is balanced by viscous dissipation ϵ_μ. The energy injected by buoyancy $\epsilon_{inj} \approx (\rho_f - \rho_b)\phi g\langle U\rangle$, where $\langle U\rangle$ is the average bubble rise velocity. Note that $\epsilon_\sigma = -\partial_t \int \sigma \, ds$ (Joseph 1976), where ds is the bubble surface element, and its contribution is zero in the steady state. The excellent agreement between steady-state values of ϵ_μ and ϵ_{inj} is evident from figure 3.

Lance & Bataille (1991) argued that the energy injected by the buoyancy is dissipated in the wakes on the bubble. The energy dissipation in the wakes can be estimated as $\epsilon_w = C_d\phi((\delta\rho/\rho_f)gd)^{3/2}/d$, where C_d is the drag coefficient. Assuming $C_d = O(1)$, we find that ϵ_w is indeed comparable to the viscous dissipation in the fluid phase $\epsilon_{\mu,f}$ (see figure 3).

3.3. *Probability distribution function of the fluid and bubble velocity fluctuations*

In figure 4(a,b) we plot the probability distribution function (p.d.f.) of the fluid velocity fluctuations $\boldsymbol{u}^f \equiv \boldsymbol{u}[c = 1]$. Both the horizontal and vertical velocity p.d.f.s are in quantitative agreement with the experimental data of Riboux *et al.* (2010) and Risso (2018). The p.d.f. of the velocity fluctuations of the horizontal velocity components are symmetric about the origin and have stretched exponential tails, whereas the vertical velocity fluctuations are positively skewed (Riboux *et al.* 2010; Prakash *et al.* 2016; Alméras *et al.* 2017). Our results are consistent with the recently proposed stochastic model of Risso (2016), which suggests that the potential flow disturbance around bubbles, bubble wakes and the turbulent agitation because of flow instabilities, together lead to the observed velocity distributions. We believe that the deviation in the tail of the distributions arises because of the differences in the wake flow for different Re and At (see figure 1). Note that positive skewness in the vertical
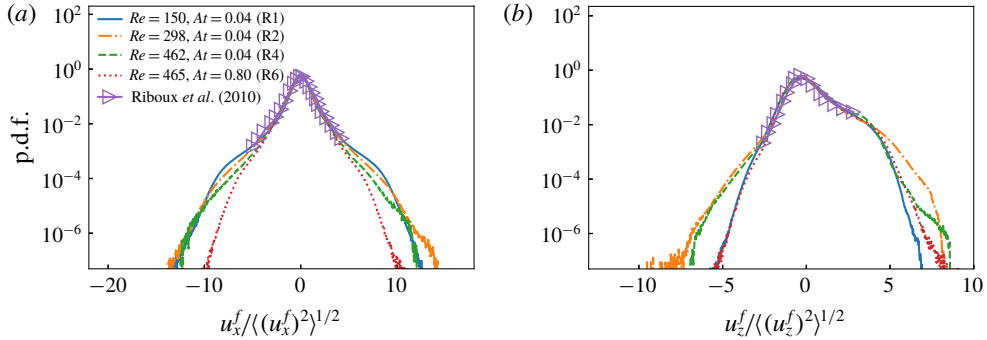
FIGURE 4. The probability distribution function of the (*a*) horizontal component and (*b*) vertical component of the liquid velocity fluctuations for runs given in table 1. The p.d.f.s obtained from our DNS are in excellent agreement with the experimental data of Riboux *et al.* (2010) (data extracted using Engauge https://markummitchell.github.io/engauge-digitizer/).
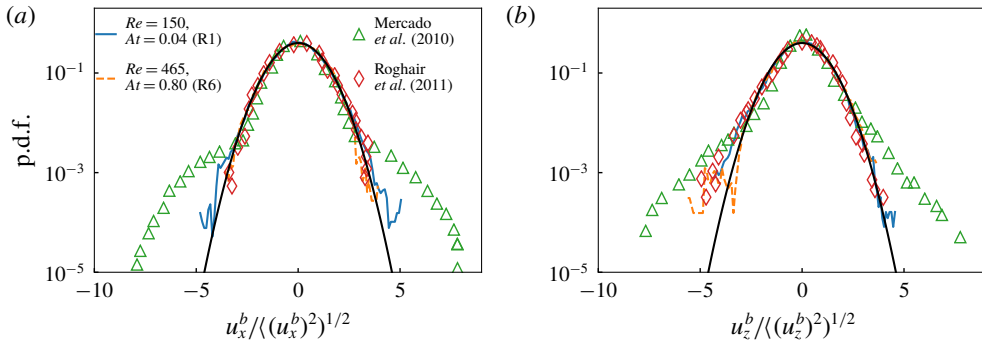

FIGURE 5. The probability distribution function of (*a*) the horizontal and (*b*) the vertical component of the bubble velocity fluctuations for runs R1 and R6 (see table 1). The experimental data of Mercado *et al.* (2010) and numerical results of Roghair *et al.* (2011) are also shown for comparison. The black continuous line represents a Gaussian distribution.

velocity has also been observed in thermal convection with bubbles (Biferale *et al.* 2012).

By tracking the individual bubble trajectories we obtain their centre-of-mass velocity $\boldsymbol{u}^b$. In agreement with the earlier simulations of Roghair *et al.* (2011), the p.d.f.s of the bubble velocity fluctuation are Gaussian (see figure 5). The departure in the tail of the distribution is most probably because of the presence of large-scale structures observed in experiments that are absent in simulations with periodic boundaries (Roghair *et al.* 2011).

3.4. *Energy spectra and scale-by-scale budget*

In the following, we study the energy spectrum

$$E_k^{uu} \equiv \sum_{k-1/2 < m < k+1/2} |\hat{\boldsymbol{u}}_m|^2, \tag{3.2}$$

the co-spectrum

$$E_k^{\rho uu} \equiv \sum_{k-1/2 < m < k+1/2} \Re[(\hat{\rho u})_{-m} \hat{u}_m] \equiv d\mathscr{E}/dk, \qquad (3.3)$$

and the scale-by-scale energy budget. Our derivation of the energy budget is similar to Frisch (1997) and Pope (2012). For a general field $f(x)$, we define a corresponding coarse-grained field (Frisch 1997) $f_k^<(x) \equiv \sum_{m \leqslant k} f_m \exp(im \cdot x)$ with the filtering length scale $\ell = 2\pi/k$. Using the above definitions in (2.1a), we get the energy budget equation

$$\partial_t \mathscr{E}_k + \Pi_k + \mathscr{F}_k^\sigma = \mathscr{P}_k - \mathscr{D}_k + \mathscr{F}_k^g. \qquad (3.4)$$

Here, $2\mathscr{E}_k = \langle u_k^< \cdot (\rho u)_k^< \rangle$ is the cumulative energy up to wavenumber k, $2\Pi_k = \langle (\rho u)_k^< \cdot (u \cdot \nabla u)_k^< \rangle + \langle u_k^< \cdot (u \cdot \nabla \rho u)_k^< \rangle$ is the energy flux through wavenumber k, $2\mathscr{D}_k = -[\langle (\rho u)_k^< \cdot (\nabla \cdot [2\mu S]/\rho)_k^< \rangle + \langle u_k^< \cdot (\nabla \cdot [2\mu S])_k^< \rangle]$ is the cumulative energy dissipated up to k, $2\mathscr{F}_k^\sigma = -[\langle (\rho u)_k^< \cdot (F^\sigma/\rho)_k^< \rangle + \langle u_k^< \cdot (F^\sigma)_k^< \rangle]$ is the cumulative energy transferred from the bubble surface tension to the fluid up to k, and $2\mathscr{F}_k^g = \langle (\rho u)_k^< \cdot (F^g/\rho)_k^< \rangle + \langle u_k^< \cdot (F^g)_k^< \rangle$ is cumulative energy injected by buoyancy up to k. In a crucial departure from the uniform density flows, we find a non-zero cumulative pressure contribution $2\mathscr{P}_k = \langle (\rho u)_k^< \cdot (\nabla p/\rho)_k^< \rangle$.

In the Boussinesq regime (small *At*), the individual terms in the scale-by-scale budget simplify to their uniform density analogues: $\mathscr{E}_k = \rho_a \langle u_k^< \cdot u_k^< \rangle/2$, $\Pi_k = \rho_a \langle u_k^< \cdot (u \cdot \nabla u)_k^< \rangle$, $\mathscr{D}_k = -\mu \langle |\nabla u_k^<|^2 \rangle$, $\mathscr{F}_k^\sigma = -\langle u_k^< \cdot (F^\sigma)_k^< \rangle$, $\mathscr{F}_k^g = \langle u_k^< \cdot (F^g)_k^< \rangle$, and $\mathscr{P}_k = 0$.

3.4.1. *Low-At (runs R1–R4)*

We first discuss the results for the Boussinesq regime (low *At*). For scales smaller than the bubble diameter ($k > k_d$), the energy spectrum (figure 6a) shows a power-law behaviour $E(k) \sim k^{-\beta}$ for different *Re*. The exponent $\beta = 4$ for $Re = 150$ – it decreases on increasing *Re* and becomes close to $\beta = 3$ for the largest value $Re = 462$.

We now investigate the dominant balances using the scale-by-scale energy budget analysis. In the statistically steady state $\partial_t \mathscr{E}_k = 0$ and $\Pi_k + \mathscr{F}_k^\sigma = -\mathscr{D}_k + \mathscr{F}_k^g$ (note that $\mathscr{P}_k = 0$ for low *At*). In figures 6(b) and 6(c) we plot different contributions to the cumulative energy budget for $Re = 150$ and $Re = 462$ and make the following observations:

(i) The cumulative energy injected by buoyancy $\mathscr{F}_k^g$ saturates around $k \approx k_d$. Thus buoyancy injects energy at scales comparable to and larger than the bubble diameter.

(ii) The energy flux $\Pi_k > 0$ around $k \approx k_d$ and vanishes for $k \gg k_d$.

(iii) Especially for scales smaller than the bubble diameter, the cumulative energy transfer from the bubble surface tension to the fluid is the dominant energy transfer mechanism.

(iv) Consistent with the earlier predictions (Riboux *et al.* 2010), for our highest $Re = 462$, simulation provides direct evidence that the balance of total production $d(\Pi_k + \mathscr{F}_k^\sigma)/dk \sim k^{-1}$ with viscous dissipation $[d\mathscr{D}_k/dk = \nu k^2 E(k)]$ gives the pseudo-turbulence spectra $E(k) \sim k^{-3}$ (Lance & Bataille 1991; Riboux *et al.* 2010; Roghair *et al.* 2011).

Our scale-by-scale analysis, therefore, suggests the following mechanism of pseudo-turbulence. Buoyancy injects energy at scales comparable to and larger than
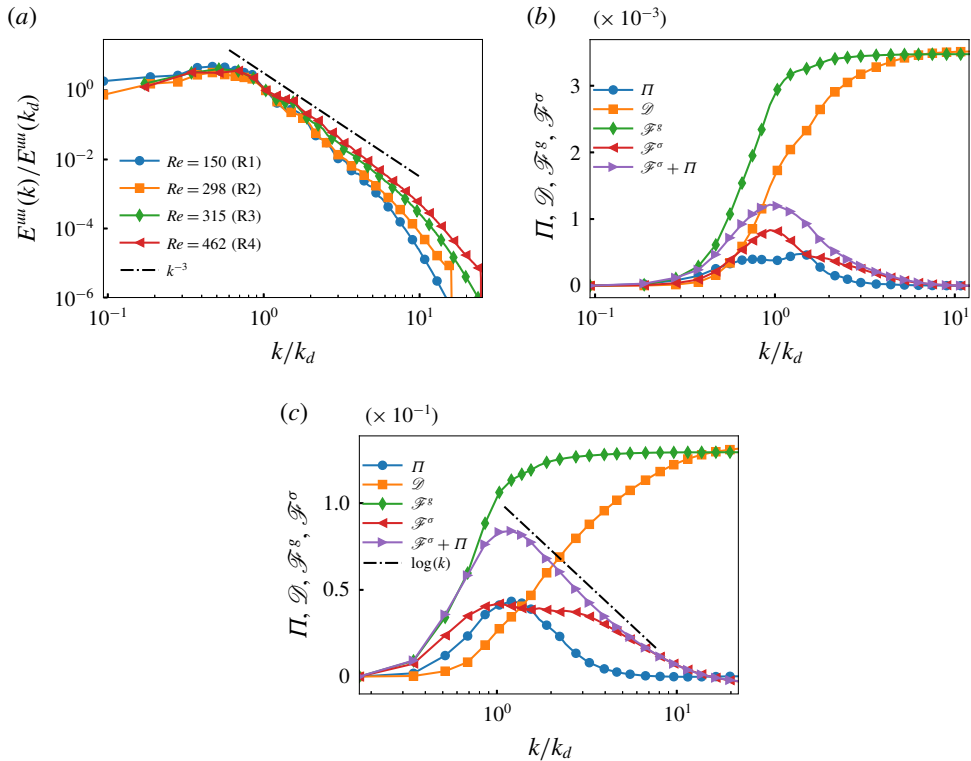
FIGURE 6. (*a*) The log–log plot of the energy spectra E_k^{uu} versus k/k_d for our high-*Re*, low-*At* runs R1–R4. Dash-dotted line indicates k^{-3} scaling. (*b, c*) Cumulative contribution of viscous dissipation $\mathscr{D}_k$, energy injected because of buoyancy $\mathscr{F}_k^g$ and the surface tension contribution $\mathscr{F}_k^\sigma$ versus k/k_d for (*b*) run R1 and (*c*) run R4. Note that, for $k > k_d$, the balance between $\mathrm{d}\mathscr{F}_k^\sigma/\mathrm{d}k$ and $\mathrm{d}\mathscr{D}_k/\mathrm{d}k$ is more prominent in (*c*) compared to (*b*).

the bubble size. A part of the energy injected by buoyancy is absorbed in stretching and deformation of the bubbles and another fraction is transferred via wakes to scales comparable to the bubble diameter. Similar to polymers in turbulent flows Perlekar, Mitra & Pandit (2006, 2010), Valente, da Silva & Pinho (2014), the relaxation of the bubbles leads to injection of energy at scales smaller than the bubble diameter.

Note that for low *At*, Boussinesq regime $\rho = \rho_a$, there is no distinction between a droplet and a bubble. Therefore, our results for low-*At* buoyancy-driven bubbly flows are equally valid for a suspension of sedimenting droplets.

3.4.2. *High-At (runs R5–R7)*

Similar to the earlier section, here also the energy spectrum and the co-spectrum show a scaling of k^{-3} at high $Re = 546$ (Roghair *et al.* 2011) and the spectrum becomes steeper $E(k) \sim k^{-3.6}$ (Bunner & Tryggvason 2002*b*) on decreasing to $Re = 173$ (figure 7*a*). However, because of density variations, the scale-by-scale energy budget becomes more complex. Now, in the statistically steady state, $\Pi_k + \mathscr{F}_k^\sigma = \mathscr{P}_k - \mathscr{D}_k + \mathscr{F}_k^g$.

In figure 7(*b*) we plot the scale-by-scale energy budget for our high-*At* run R6. We find that the cumulative energy injected by buoyancy and the pressure contribution
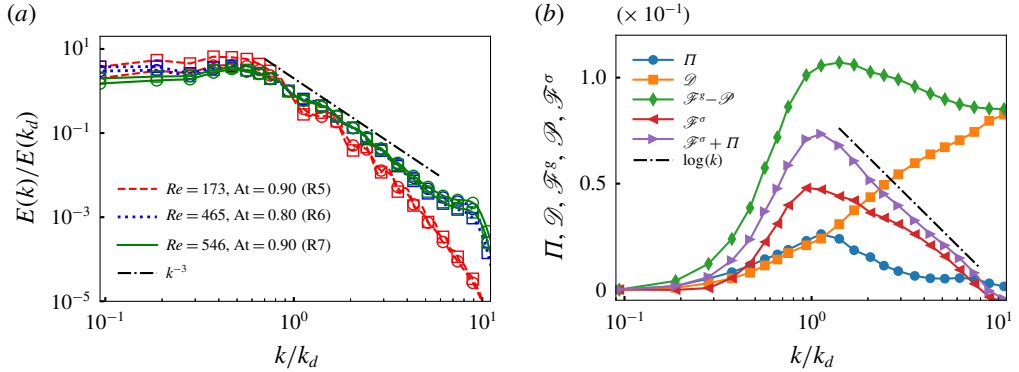
FIGURE 7. (*a*) The log–log plot of the energy spectra (○) E_k^{uu} and co-spectrum (□) $E_k^{\rho uu}$ versus k/k_d for our high-*Re*, high-*At* runs R5–R7. Dash-dotted line indicates k^{-3} scaling. (*b*) Cumulative contribution of the viscous dissipation $\mathscr{D}_k$, the contribution due to buoyancy and pressure $\mathscr{F}_k^g$–$\mathscr{P}_k$, the energy flux Π_k and the surface-tension contribution $\mathscr{F}_k^\sigma$ versus k/k_d for run R6.

$\mathscr{F}_k^g + \mathscr{P}_k$ reaches a peak around $k \approx k_d$ and then decrease mildly to ϵ_{inj}. Similar to the low-*At* case, we find a non-zero energy flux for $k \approx k_d$ and a dominant surface-tension contribution to the energy budget for $k \gg k_d$. Finally, similar to the previous section, for $k > k_d$ the net production $\mathrm{d}(\Pi + \mathscr{F}^\sigma)/\mathrm{d}k \sim k^{-1}$ balances the viscous dissipation $\nu k^2 E(k)$ to give $E(k) \sim k^{-3}$.

3.4.3. *Frequency spectrum of pseudo-turbulence*

To investigate the frequency spectrum of pseudo-turbulence, we now conduct a time-series analysis similar to Roghair *et al.* (2011) and Prakash *et al.* (2016) for our high $At = 0.8$, high $Re = 465$ run R6. We monitor the time evolution of the three components of the velocity and the density ρ for time $T = 90\tau_\lambda$, with sampling time $8 \times 10^{-3}\tau_\lambda$, on 32^3 equally spaced Eulerian points within our simulation domain. From these signals, we select continuous segments of liquid velocity fluctuations of size $T_s \geqslant 19\tau_\lambda$ and ignore regions where $\rho = \rho_b$. We then use the Welch method, with Hamming windows, to obtain the energy spectrum (Welch 1967; Prakash *et al.* 2016). In figure 8(*a*) we plot the liquid velocity spectrum $E(\nu)$ versus ν/ν_d and find it to be in excellent agreement with the experiments of Prakash *et al.* (2016). In figure 8(*b*) we show that the normalized energy spectrum is not modified on doubling $T_s \geqslant 38\tau_\lambda$. Similar to Roghair *et al.* (2011), Prakash *et al.* (2016) and Alméras *et al.* (2017) we find that $E(\nu) \sim \nu^{-3}$ for frequencies $\nu > \nu_d$, where $\nu_d = \langle U \rangle/2\pi d$ (Prakash *et al.* 2016).

3.5. *Length scales of pseudo-turbulence*

We have used bubble diameter as a relevant scale of pseudo-turbulence (Mendez-Diaz *et al.* 2013; Prakash *et al.* 2016). Riboux *et al.* (2010) proposed an alternative length scale $\Lambda \propto V_0^2/g = 4\delta\rho d/(3\rho_f C_{d0})$, where V_0 is the single bubble rise velocity and C_{d0} is the drag coefficient of an isolated bubble. Note that for large *At*, $\delta\rho/\rho_f \approx 1$. In table 2 we present values of d and Λ obtained from our numerical simulations R1–R7. For our large-*At* runs, we find that bubble diameter is comparable to Λ ($d/\Lambda \approx 0.4$–0.6). On the other hand, for our small-*At* runs, $d/\Lambda \approx 4$–6, indicating that k_Λ/k_d lies near
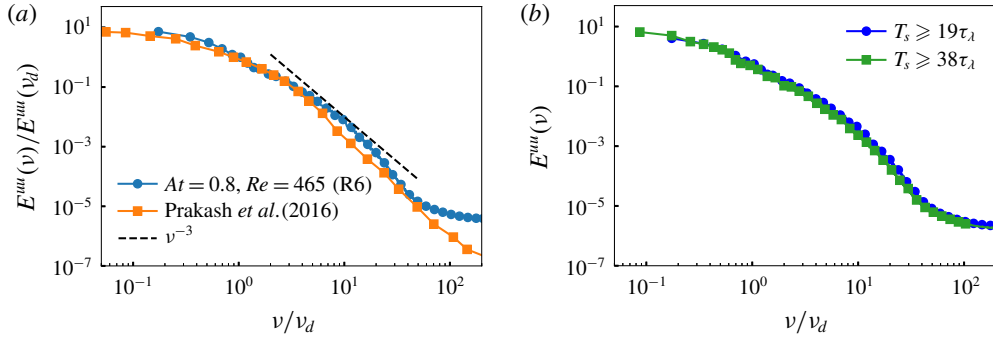
FIGURE 8. (*a*) Kinetic energy spectrum of the liquid velocity fluctuations $E(\nu)$ versus ν/ν_d for our run R6. We also overlay the spectrum obtained from the experiments of Prakash *et al.* (2016) and find it to be in excellent agreement with our numerical simulation. (*b*) Comparison of the normalized energy spectrum obtained from liquid velocity segments of length $T_s \geqslant 19\tau_\lambda$ (1.9×10^4 trajectories) and $38\tau_\lambda$ (5×10^3 trajectories).

runs	R1	R2	R3	R4	R5	R6	R7
Λ	4.0	6.2	4.1	4.3	52.9	38.4	53.3
d/Λ	6.0	3.8	5.4	5.1	0.5	0.6	0.4

TABLE 2. Length scale $\Lambda \propto V_0^2/g = 4\delta\rho d/(3\rho_f C_{d0})$ and the ratio d/Λ for our runs R1–R7.

the end of the k^{-3} scaling range. Thus Λ does not capture the beginning of the k^{-3} scaling for our low-*At* runs.

3.6. *Clustering of bubbles*

Using Voronoi analysis, Tagawa *et al.* (2013) investigated clustering in bubbly flows with varying *Re*, surface tension σ and d/L for $\phi = 5\%$–40 %. They observed that the clustering depends on the deformability of the bubbles. To investigate clustering in our numerical study on dilute bubbly flows ($\phi = 1.7\%$–2.6 %), we repeated the analysis of Tagawa *et al.* (2013) for our runs R1–R7. From the bubble centre-of-mass positions, we construct Voronoi tesselations using the Voro++ library (Rycroft 2009). We then evaluate the standard deviation Σ of the Voronoi volumes obtained from the steady-state bubble configurations. We also generate 200 configurations of randomly positioned, non-overlapping, N_b bubbles of diameter d in a box of length L. Using the Voronoi tesselation of these random configurations, we evaluate the standard deviation Σ_{rnd}. The ratio $\mathcal{C} \equiv \Sigma/\Sigma_{rnd}$ gives an indication of the bubble clustering. Note that $\mathcal{C} < 1$ for a regular lattice arrangement, $\mathcal{C} = 1$ for a random arrangement, and $\mathcal{C} > 1$ for irregular clustering (Tagawa *et al.* 2013). We observe random or weakly irregular clustering for our runs R1–R6 (see table 3). For our high-*Re*, high-*At* run R7, $\mathcal{C} = 0.9$, which indicates a weakly regular lattice arrangement of bubbles. Therefore, for our simulations with $\phi = 1.7\%$–2.6 %, we do not observe any systematic effect of clustering on the energy spectrum.

runs	R1	R2	R3	R4	R5	R6	R7
$\mathcal{C}$	1.3	1.3	1.1	1.1	1.3	1.0	0.9

TABLE 3. The clustering indicator $\mathcal{C}$ for our runs R1–R7.

4. Conclusion

To conclude, we have investigated the statistical properties of velocity fluctuations in pseudo-turbulence generated by buoyancy-driven bubbly flows. The *Re* values that we have explored are consistent with the range $Re \sim [300\text{--}1000]$ used in the experiments (Riboux *et al.* 2010; Mendez-Diaz *et al.* 2013; Prakash *et al.* 2016). Our numerical simulations show that the shape of the p.d.f. of the velocity fluctuations is consistent with experiments over a wide range of *Re* and *At* numbers. For large *Re*, and for low as well as high *At*, the energy spectrum shows a $E(k) \sim k^{-3}$ scaling (Roghair *et al.* 2011). However, on reducing *Re*, the spectrum becomes steeper $E(k) \sim k^{-4}$ (Bunner & Tryggvason 2002*b*). We observe a non-zero positive energy flux for scales comparable to the bubble diameter. Our scale-by-scale energy budget validates the theoretical prediction that the net production balances viscous dissipation to give $E(k) \sim k^{-3}$.

Experiments on pseudo-turbulence have investigated the liquid velocity fluctuations either within the bubble swarm (Larue De Tournemine 2001; Mercado *et al.* 2010; Mendez-Diaz *et al.* 2013; Prakash *et al.* 2016) or in the wake of the bubble swarm (Riboux *et al.* 2010). All these experiments show a robust -3 spectrum. However, Riboux *et al.* (2010) also observed that the -3 spectrum is followed by nearly half a decade of $-5/3$ spectrum. A similar observation, albeit for a much smaller scaling range, was also made by Mendez-Diaz *et al.* (2013). Consistent with bubble swarm experiments (Larue De Tournemine 2001; Mercado *et al.* 2010; Prakash *et al.* 2016), we do not observe a $-5/3$ spectrum. A plausible reason for the observed discrepancy, as indicated by Riboux *et al.* (2010), could be that strong flows generated in the vicinity of the bubbles are absent in the wake of the bubble swarm.

Acknowledgements

Supplementary movies

Supplementary movies are available at https://doi.org/10.1017/jfm.2019.991.

References

ALMÉRAS, E., MATHAI, V., SUN, C. & LOHSE, D. 2019 Mixing induced by a bubble swarm rising through incident turbulence. *Intl J. Multiphase Flow* **114**, 316–322.

ALMÉRAS, E., MATHAI, V., LOHSE, D. & SUN, C. 2017 Experimental investigation of the turbulence induced by a bubble swarm rising within incident turbulence. *J. Fluid Mech.* **825**, 1091–1112.

ANISZEWSKI, W. *et al.* 2019 PArallel, Robust, Interface Simulator (PARIS), hal-02112617. Available at: https://hal.sorbonne-universite.fr/hal-02112617.

BHAGA, D. & WEBER, M. E. 1981 Bubbles in viscous liquids: shapes, wakes and velocities. *J. Fluid Mech.* **105**, 61–85.

BIFERALE, L., PERLEKAR, P., SBRAGAGLIA, M. & TOSCHI, F. 2012 Convection in multiphase fluid flows using lattice Boltzmann methods. *Phys. Rev. Lett.* **108**, 104502.

BUNNER, B. & TRYGGVASON, G. 2002*a* Dynamics of homogeneous bubbly flows. Part 1. Rise velocity and microstructure of the bubbles. *J. Fluid Mech.* **466**, 17–52.

BUNNER, B. & TRYGGVASON, G. 2002*b* Dynamics of homogeneous bubbly flows. Part 2. Velocity fluctuations. *J. Fluid Mech.* **466**, 53–84.

CANUTO, C., HUSSAINI, M. Y., QUARTERONI, A. M. & ZANG, T. A. 2012 *Spectral Methods in Fluid Dynamics*. Springer-Verlag.

CECCIO, S. L. 2010 Friction drag reduction of external flows with bubble and gas injection. *Annu. Rev. Fluid Mech.* **42**, 183–202.

CLIFT, R., GRACE, J. R. & WEBER, M. E. 1978 *Bubbles, Drops and Particles*. Academic Press.

DECKWER, W.-D. 1992 *Bubbles Column Reactors*. Wiley.

ELGHOBASHI, S. 2019 Direct numerical simulation of turbulent flows laden with droplets or bubbles. *Annu. Rev. Fluid Mech.* **51**, 217–244.

FRISCH, U. 1997 *Turbulence, A Legacy of A. N. Kolmogorov*. Cambridge University Press.

GONNERMANN, H. M. & MANGA, M. 2007 The fluid mechanics inside a volcano. *Annu. Rev. Fluid Mech.* **39**, 321–356.

JOSEPH, D. D. 1976 *Stability of Fluid Motions II*. Springer.

LANCE, M. & BATAILLE, J. 1991 Turbulence in the liquid phase of a uniform bubbly airwater flow. *J. Fluid Mech.* **222**, 95–118.

LARUE DE TOURNEMINE, A. 2001 Etude expérimentale de l'effet du taux de vide en écoulement diphasique á bulles. PhD thesis, Institut National Polytechnique de Toulouse.

MATHAI, V., HUISMAN, S. G., SUN, C., LOHSE, D. & BOURGOIN, M. 2018 Dispersion of air bubbles in isotropic turbulence. *Phys. Rev. Lett.* **121** (5), 054501.

MATHAI, V., LOHSE, D. & SUN, C. 2020 Bubble and buoyant particle laden turbulent flows. *Annu. Rev. Condens. Matter Phys.* **11**, (in press).

MENDEZ-DIAZ, S., SERRANO-GARCIA, J. C., ZENIT, R. & HERNÁNDEZ-CORDERO, J. A. 2013 Power spectral distributions of pseudo-turbulent bubbly flows. *Phys. Fluids* **25** (4), 043303.

MERCADO, J. M., GÓMEZ, D. G., GILS, D. V., SUN, C. & LOHSE, D. 2010 On bubble clustering and energy spectra in pseudo-turbulence. *J. Fluid Mech.* **650**, 287–306.

MUDDE, R. F. 2005 Gravity-driven bubbly flows. *Annu. Rev. Fluid Mech.* **37**, 393–423.

PANDIT, R. *et al.* 2017 An overview of the statistical properties of two-dimensional turbulence in fluids with particles, conducting fluids, fluids with polymer additives, binary-fluid mixtures, and superfluids. *Phys. Fluids* **29**, 111112.

PANDIT, R., PERLEKAR, P. & RAY, S. S. 2009 Statistical properties of turbulence: an overview. *Pramana* **73** (1), 157–191.

PERLEKAR, P. 2019 Kinetic energy spectra and flux in turbulent phase-separating symmetric binary-fluid mixtures. *J. Fluid Mech.* **873**, 459–474.

PERLEKAR, P., MITRA, D. & PANDIT, R. 2006 Manifestations of drag reduction by polymer additives in decaying, homogeneous, isotropic turbulence. *Phys. Rev. Lett.* **97**, 264501.

PERLEKAR, P., MITRA, D. & PANDIT, R. 2010 Direct numerical simulations of statistically steady, homogeneous, isotropic fluid turbulence with polymer additives. *Phys. Rev.* E **82**, 066313.

PIVELLO, M. R., VILLAR, M. M., SERFATY, R., ROMA, A. M. & SILVEIRA-NETO, A. 2014 A fully adaptive front tracking method for the simulation of two phase flows. *Intl J. Multiphase Flow* **58**, 72–82.

POPE, S. 2012 *Turbulent Flows*. Cambridge University Press.

PRAKASH, V. N., MERCADO, J. M., VAN WIJNGAARDEN, L., MANCILLA, E., TAGAWA, Y., LOHSE, D. & SUN, C. 2016 Energy spectra in turbulent bubbly flows. *J. Fluid Mech.* **791**, 174–190.

RIBOUX, G., RISSO, F. & LEGENDRE, D. 2010 Experimental characterization of the agitation generated by bubbles rising at high Reynolds number. *J. Fluid Mech.* **643**, 509–539.

RISSO, F. 2011 Theoretical model for k^{-3} spectra in dispersed multiphase flows. *Phys. Fluids* **23** (1), 011701.

RISSO, F. 2016 Physical interpretation of probability density functions of bubble-induced agitation. *J. Fluid Mech.* **809**, 240–263.

RISSO, F. 2018 Agitation, mixing, and transfers induced by bubbles. *Annu. Rev. Fluid Mech.* **50**, 25–48.

ROGHAIR, I., MERCADO, J. M., ANNALAND, M. V. S., KUIPERS, H., SUN, C. & LOHSE, D. 2011 Energy spectra and bubble velocity distributions in pseudo-turbulence: numerical simulations versus experiments. *Intl J. Multiphase Flow* **37** (9), 1093–1098.

RYCROFT, C. H. 2009 Voro++: a three-dimensional Voronoi cell library in C++. *Chaos: An Interdisciplinary Journal of Nonlinear Science* **19** (4), 041111.

SHUKLA, I., KOFMAN, N., BALESTRA, G., ZHU, L. & GALLAIRE, F. 2019 Film thickness distribution in gravity-driven pancake-shaped droplets rising in a Hele-Shaw cell. *J. Fluid Mech.* **874**, 1021–1040.

TAGAWA, Y., ROGHAIR, I., PRAKASH, V. N., VAN SINT ANNALAND, M., KUIPERS, H., SUN, C. & LOHSE, D. 2013 The clustering morphology of freely rising deformable bubbles. *J. Fluid Mech.* **721**, R2.

TCHOUFAG, J., MAGNAUDET, J. & FABRE, D. 2014 Linear instability of the path of a freely rising spheroidal bubble. *J. Fluid Mech.* **751**, R4.

TRIPATHI, M. K., SAHU, K. C. & GOVINDARAJAN, R. 2015 Dynamics of an initially spherical bubble rising in quiescent liquid. *Nat. Commun.* **6**, 6268.

TRYGGVASON, G., BUNNER, B., ESMAEELI, A., JURIC, D., AL-RAWAHI, N., TAUBER, W., HAN, J., NAS, S. & JAN, Y.-J. 2001 A front-tracking method for the computations of multiphase flow. *J. Comput. Phys.* **169** (2), 708–759.

VALENTE, P. C., DA SILVA, C. B. & PINHO, F. T. 2014 The effect of viscoelasticity on the turbulent kinetic energy cascade. *J. Fluid Mech.* **760**, 39–62.

WELCH, P. 1967 The use of fast Fourier transform for the estimation of power spectra: a method based on time averaging over short, modified periodograms. *IEEE Trans. Audio Electroacoust.* **15** (2), 70–73.

WU, M. & GHARIB, M. 2002 Experimental studies on the shape and path of small air bubbles rising in clean water. *Phys. Fluids* **14** (7), L49–L52.